

Charge Transfer Parameters of $\text{Ni}_x\text{Mn}_y\text{Co}_{1-x-y}$ Cathodes Evaluated by a Transmission Line Modeling Approach

Janina Costard, Jochen Joos,* Adrian Schmidt, and Ellen Ivers-Tiffée*

The performance of lithium-ion batteries can be analyzed and improved by appropriate electrochemical models. A challenging yet crucial part is the parameterization of these models. Until now, the literature has incompletely investigated and cited the charge transfer process parameters describing the lithium transfer between the active material particles in the electrode and the liquid electrolyte. Herein, a novel approach is presented for obtaining these charge transfer parameters. The well-established experimental methods of electrochemical impedance spectroscopy and focused ion beam tomography are applied. By introducing both experimental results into a transmission line model, a reliable determination of the charge transfer parameters j_0 , k , and r_{CT} can be achieved. The new approach is validated by comparing the results of four cathodes, all containing the state-of-the-art active material $\text{Ni}_x\text{Mn}_y\text{Co}_{1-x-y}$ (NMC), but with different microstructures and/or stoichiometries.

R_{CT} , of any processed cathode sheet is given by its stoichiometry, phase composition, and microstructure characteristics. In contrast, the *area-specific* charge transfer resistance, r_{CT} , describes the performance of the cathode active material itself, and scales with the volume-specific active surface area, $a_{\text{AM,act}}$, that is available for the lithium ions to be intercalated within the active material. Furthermore, the necessary material properties described by the parameter exchange current density, j_0 , or reaction rate, k , are of utmost importance for performance modeling, as can be seen in previous studies.^[2–6] The discrepancies between the parameter values provided in the literature are still an obstacle. Indeed, solid solutions based on $\text{Ni}_x\text{Mn}_y\text{Co}_{1-x-y}$ (NMC) are highly interest-

ing for lithium-ion batteries due to an excellent balance between capacity, rate capability, voltage, and energy density; sadly these model parameters are rarely found in the literature.

Figure 1 introduces our approach for disclosing at least the earlier introduced parameters r_{CT} , j_0 , and k , using experimentally determined parameters from focused ion beam (FIB)/scanning electron microscopy (SEM) tomography, conductivity measurements, and electrochemical impedance spectroscopy (EIS) combined with a transmission line model (TLM) for porous electrodes.

FIB/SEM tomography was successfully applied by our group for research on lithium-ion-battery electrodes,^[7,8] separating and quantitatively analyzing the active material phase, pore phase, and carbon black/binder phase. Earlier studies failed to detect the carbon black/binder phase, which in turn led to an overestimation of the active area $A_{\text{AM,act}}$ of the active material within the cathode sheet. Alternative approaches reported in the literature later bypassed this challenge by calculating the active surface area from a measured particle size distribution^[9] or by assuming a planar surface for a thin-film electrode.^[10]


EIS determines the sum of impedance contributions for the investigated cathode sheet without unwanted artifacts from the counter electrode, when a three-electrode setup is used.^[11,12] As already demonstrated in 1960,^[13] the charge transfer resistance, R_{CT} , can then be evaluated using a suitable TLM. A TLM is an equivalent circuit model that respects the porous structure of a lithium-ion-battery electrode, wherein the open pore space is filled with liquid electrolyte. But a reliable TLM model fit ultimately requires the cathode microstructure parameter values for porosity ϵ , tortuosity τ , and active surface area $A_{\text{AM,act}}$, the electrode thickness L , and the conductivity of the ionic and the electronic transport path, as well as the total

1. Introduction

Battery systems based on porous intercalation electrodes (such as commercial lithium-ion batteries) are receiving growing attention because of their potentially high energy and power densities. For further optimizing and understanding their performance, electrochemical models are applied (such as the well-known Newman model^[1]). These are based on fundamental equations describing migration, diffusion, and intercalation kinetics.

A crucial aspect of the model validity is parameterizing these equations. This work aims to support parameterization, as it introduces a new approach for evaluating the parameters of the charge transfer kinetics at the interface between the active cathode material and the liquid electrolyte, usually described by the Butler–Volmer equation. The charge transfer resistance,

Dr. J. Costard, Dr. J. Joos, A. Schmidt, Prof. E. Ivers-Tiffée
Institute for Applied Materials – Materials for Electrical and Electronic Engineering (IAM-WET)
Karlsruhe Institute of Technology (KIT)
Adenauerring 20b, Karlsruhe 76131, Germany
E-mail: jochen.joos@kit.edu; ellen.ivers-tiffée@kit.edu

 The ORCID identification number(s) for the author(s) of this article can be found under <https://doi.org/10.1002/ente.202000866>.

© 2021 The Authors. Energy Technology published by Wiley-VCH GmbH. This is an open access article under the terms of the Creative Commons Attribution-NonCommercial-NoDerivs License, which permits use and distribution in any medium, provided the original work is properly cited, the use is non-commercial and no modifications or adaptations are made.

DOI: 10.1002/ente.202000866

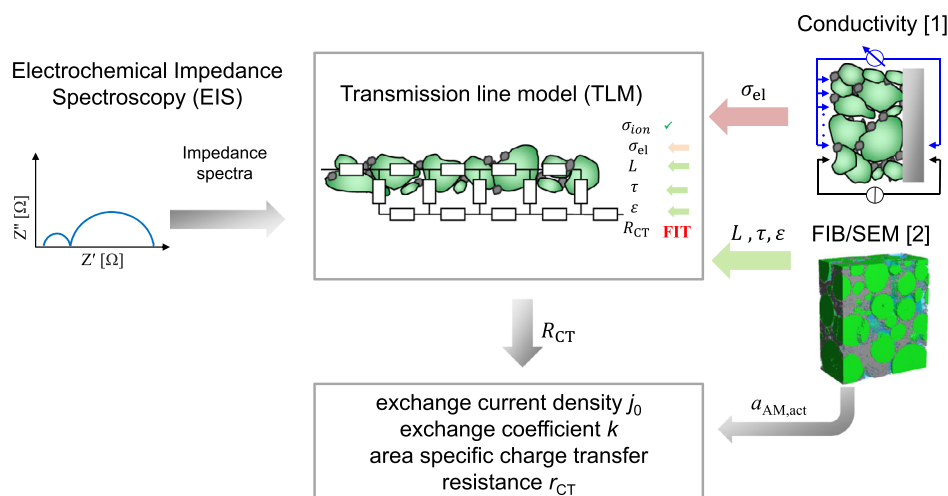


Figure 1. Approach of this study: The impedance of the cathode is measured by EIS and evaluated by the TLM; microstructure parameters are obtained by FIB/SEM tomography and conductivity is measured and applied to the model. Finally, the area-specific charge transfer resistance r_{CT} , the exchange current density j_0 , and the exchange coefficient k are calculated.

impedance of the cathode sheet under test. If these preconditions are fulfilled, the subsequent fitting procedure delivers the charge transfer resistance R_{CT} . This parameter is scaled by the active surface area, $A_{AM,act}$, obtained by FIB tomography, and yields the area-specific charge transfer resistance r_{CT} . Finally, the exchange current density, j_0 , and the exchange coefficient, k , of the active material NMC can be calculated, as shown subsequently.

This work demonstrates the validity of our new approach for cathodes made of the active material NMC with differing stoichiometries and with different microstructure characteristics (see Table 1).

2. Theory of Charge Transfer Kinetics

The Butler–Volmer equation, one of the most fundamental relationships in electrochemical kinetics, is presented in Equation (1).^[14] In this work, it is applied for describing the charge transfer kinetics at the interface between the active material of the NMC cathode samples S1 to S4 and the liquid electrolyte

$$j_{CT} = j_0 \left[\exp \left((1 - \alpha) \cdot \frac{nF\eta_{CT}}{RT} \right) - \exp \left((-\alpha) \cdot \frac{nF\eta_{CT}}{RT} \right) \right] \quad (1)$$

For linear conditions, i.e., for small currents and current amplitudes applied during EIS, Equation (1) can be simplified

Table 1. Examined cathode samples S1, S2, S3, and S4 with different microstructures, stoichiometries, and capacities.

Sample	Stoichiometry	Capacity [mAh cm ⁻²]	18 650/Sheets
S1	N _{1/3} M _{1/3} C _{1/3}	1.0	Sheets
S2	N _{0.6} M _{0.2} C _{0.2} + N _{1/3} M _{1/3} C _{1/3}	2.0	18 650
S3	N _{0.6} M _{0.2} C _{0.2}	3.9	Sheets
S4	N _{0.6} M _{0.2} C _{0.2}	6.9	Sheets

$$j_{CT} = j_0 \frac{nF\eta_{CT}}{RT} \quad (2)$$

and the area-specific charge transfer resistance r_{CT} can be calculated

$$r_{CT} = \frac{\eta_{CT}}{j_{CT}} = \frac{1}{j_0} \cdot \frac{RT}{F} \quad (3)$$

wherefrom the exchange current density j_0 can be derived, if the parameters charge transfer resistance R_{CT} and active surface area of the active material $A_{AM,act}$ of the sample under test are known (or are measurable by experiment)

$$j_0 = \frac{1}{R_{CT} \cdot A_{AM,act}} \cdot \frac{RT}{F} \quad (4)$$

Furthermore, the exchange coefficient k can be determined as a function of lithium concentration in the active material c_s and electrolyte c_l

$$k = \frac{j_0}{F} \cdot c_l^{-\alpha} \cdot c_s^{\alpha-1} \cdot \left(1 - \frac{c_s}{c_{s,max}} \right)^{-\alpha} \quad (5)$$

with $F = 96485.332 \text{ A s mol}^{-1}$.

For the calculations, $\alpha = 0.5$, $c_l = 1000 \text{ mol m}^{-3}$, and $c_s/c_{s,max} = 0.45$ are used, representing the lithiation at an electrode state of charge (SOC) of 100%,^[15] wherein $c_{s,max} = 52\,602 \text{ mol m}^{-3}$ applies for (N_{1/3}M_{1/3}C_{1/3}) and $c_{s,max} = 52\,869 \text{ mol m}^{-3}$ for N_{0.6}M_{0.2}C_{0.2}. The maximum lithium concentrations $c_{s,max}$ of the active materials were experimentally determined via transmission electron microscopy at the fully lithiated state ($\hat{=}$ SOC 0%). Diffraction images were used to determine the lattice parameters of the rhombohedral crystal lattice,^[16] from which the volume of a single cell, containing three lithium atoms in the fully lithiated state, can be determined, representing the reciprocal of a third of the maximum lithium concentration of the particular material.

Section 3 describes the experimental approach for determining the parameters of $A_{AM,act}$ and R_{CT} , and the calculations of r_{CT} , j_0 , and k are shown in Section 4.

3. Experimental Section

3.1. NMC Cathode Sheet Stoichiometry

The active material NMC is frequently used due to its good balancing between capacity, rate capability, voltage, and energy density. Specific characteristics can be designed by the stoichiometry nickel:manganese:cobalt. The standard composition $Ni_{1/3}Mn_{1/3}Co_{1/3}$ provides a reversible capacity of 163 mAh g^{-1} ; increasing nickel content leads to a capacity above 200 mAh g^{-1} for $Ni_{0.6}Mn_{0.2}Co_{0.2}$. High nickel content also promotes the electronic conductivity and lithium-ion diffusivity. The drawbacks of high nickel content are inferior thermal stability and oxygen release.^[17] The parameters r_{CT} , j_0 , and k and their dependence on stoichiometry have rarely been published or explored so far.

Table 1 shows the four different cathodes, providing different stoichiometries and microstructure characteristics. S1, S3, and S4 were available as single-phase and single-side-coated cathode sheets, whereas the blended cathode sample S2 was extracted from a commercial 18 650 lithium-ion cell. The latter was gained by removing the coating in NMP on one side and cleaning in a dimethyl carbonate + ethyl methyl carbonate (DMC:EMC 1:1 w:w) solution.

In the best case, the new approach herein was validated with regard to reproducibility, as S3 and S4 are of the same nominal stoichiometry $N_{0.6}M_{0.2}C_{0.2}$ and thus the charge transfer parameters should be identical. Moreover, the influence of small stoichiometry changes can be analyzed, as S1 is made of $N_{1/3}M_{1/3}C_{1/3}$ and S2 is a blend of $N_{0.6}M_{0.2}C_{0.2} + N_{1/3}M_{1/3}C_{1/3}$.

3.2. FIB/SEM Tomography

FIB/SEM tomography as a high-resolution 3D technique has already proven potential for quantifying the microstructural features of lithium-ion cathodes.^[8,18,19] By combining FIB milling and SEM with image processing, multiphase microstructure data are obtained with high resolution and contrast. In this work, four samples (S1–S4) were analyzed with a ZEISS 1540 XB CrossBeam (Carl Zeiss Microscopy GmbH, Oberkochen, Germany).

The experimental procedure and image processing applied in this work are extensively described in previous studies,^[7,20] for lithium-ion cathodes in particular in Almar et al.,^[8] and are shown in Figure 2.

3.2.1. Sample Preparation

A small piece of the porous cathode layer ($\approx 5 \times 5 \text{ mm}^2$) was filled with a two-component silicone rubber from Wacker (ELASTOSIL RT 675) under vacuum conditions. This resin provides mechanical stability and, later on, enables a reliable segmentation of the three phases 1) pore space, 2) carbon black, and 3) active material^[7] from SEM data. The infiltrated sample was cured for 24 h, embedded into an epoxy resin

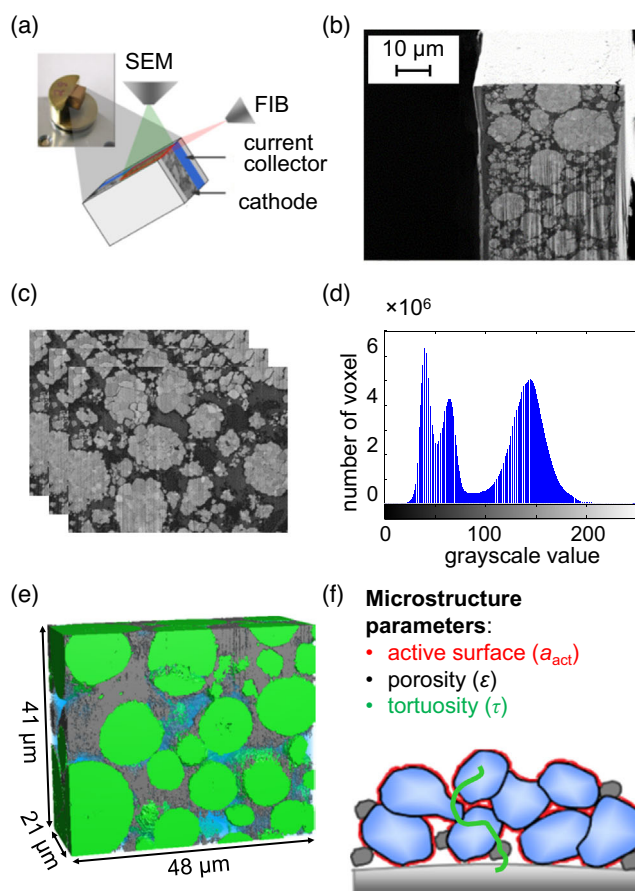


Figure 2. FIB/SEM procedure. a) setup with an FIB and an electron beam (SEM) arranged at 54° . b) Examined cathode volume: A trench was milled left and right of the region of interest. c) Image stack acquired by an alternating procedure of FIB slicing and SEM imaging. d) Histogram of grayscale values of examined volume. e) Reconstructed volume: Three phases are separated—active material (green), carbon black (gray), and pore (transparent blue). f) Obtained microstructure parameters.

(Struers EpoFix), and finished with SiC polishing papers down to a finish of $<1 \mu\text{m}$. Grinding and polishing were done with two cross-sections perpendicular to each other, which gave a clear edge. This enabled FIB/SEM sectioning right from the edge of the sample. Finally, the sample was fixed on a pin by silver conductive varnish and sputter coated by a thin gold layer ($\approx 100 \text{ nm}$) to avoid electrical charging.

3.2.2. Milling and Imaging

A trench was milled by Ga ions, followed by milling thin sections from the exposed sample surface using a 2 nA milling current, simultaneously imaged by SEM at 1.3 keV. Sequential milling and imaging yielded a serial set of consecutive SEM images of the cathode (Figure 2b,c).^[19,20]

3.2.3. Segmentation and Filtering

First, all SEM images (between 328 and 600 for S1–S4) were aligned using the ImageJ software. After a median noise filtering,

the data set was segmented on the basis of the grayscale values of all individual pixels. For this work, a global threshold method was applied for segmentation. The data quality of the images is crucial, and frequent errors are insufficient resolution, streaking on the FIB polished surface, and brightness gradients among the SEM stacks, which must be avoided.^[21,22] Comparison of original FIB polished images and segmented images (see **Figure 3**, 7, and 8) indicated accurate segmentation and filtering.

3.2.4. Microstructure Parameters

By this procedure, a 3D reconstruction of the analyzed cathode volume was derived. This data set of voxels (volumetric pixels) contains essential microstructure parameters: 1) active surface area $a_{AM,act}$, 2) porosity fraction ϵ , and 3) tortuosity τ of the pore space. The porosity fraction is calculated by simply dividing the number of voxels assigned as “pore” by the total number of voxels. The volume-specific electrochemically active surface area $a_{AM,act}$ is calculated using the marching cube algorithm, which approximates the surface area using the information of eight neighboring voxels.^[22] The tortuosity τ of the pore phase is calculated by solving the transport equation directly on the 3D data set by using a finite volume scheme in MATLAB presented in Ender et al.^[23]

As stated in the Introduction, the microstructure parameters of lithium-ion cathodes show features on different length scales (see example S4 in **Figure 3**). NMC agglomerates with diameters over 10 μm exist, which require analyzing a sufficiently large, representative volume. On the other hand, the nanosized carbon black and small pores or cracks inside the active material require a sufficiently high resolution, small pixel size, and slice thickness, respectively. Herein a compromise was made between

those conflictive requirements.^[8] The pixel size of 30–45 nm accurately resolved carbon black and small pores inside NMC, as the enlarged section in **Figure 3** shows, thus ensuring an accurate analysis of the reconstructed volumes. The slice thickness was chosen to the same value for obtaining cubic voxels. For determining the maximal possible resolution without loss of information, different resolutions were tested.

The reconstructed volumes in this work amounted to 10 071–41 328 μm^3 , which are among the largest reconstructions with comparable pixel size and slice thickness via FIB tomography reported in the literature (e.g., 4500 μm^3 with a slice thickness of 62 nm,^[24] 28 100 μm^3 with a slice thickness of 200 nm,^[18] and 42 395 μm^3 with a slice thickness of 150 nm^[25]).

3.3. EIS and Conductivity Measurements

EIS was conducted on samples S1–S4. A three-electrode setup was used with a $\text{Li}_4\text{Ti}_5\text{O}_{12}$ (LTO)-coated aluminum mesh as the reference electrode ($d = 21$ mm) placed between two glass fiber separators symmetrically between the working and counter electrode (see **Figure 4**). This reference electrode design was developed to provide an error-free impedance spectra in half-cell setups.^[11,12] The working electrodes were the four investigated NMC cathodes ($d = 18$ mm) and a lithium metal foil ($d = 18$ mm) was used as the counter electrode. The electrolyte is based on an EC:DMC (1:1 w:w) solvent mixture and contains 1 M LiPF_6 as conducting salt.

All measurements were conducted using a Solartron 1470E cell test system with Scribner Multistat software. The sample under test, measured at 4.2 V, which equals a 100% SOC and lithiation ($c_s/c_{s,max}$) of 0.45,^[15] was equilibrated for 5 h at a standard temperature of 25 °C, adjusted and controlled by a

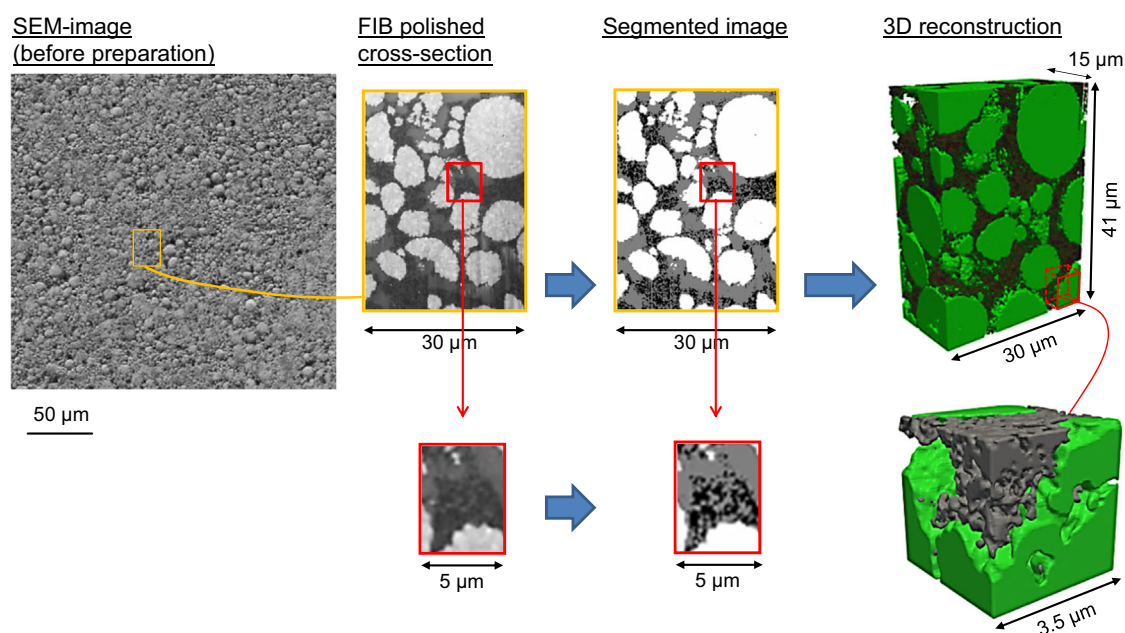


Figure 3. SEM image of sample S4 with one FIB slice of the reconstructed volume, the corresponding segmented image, and the reconstructed 3D volume. Furthermore, a zoom of the carbon black domain is shown. This demonstrates the different length scales that occur inside a battery cathode and have to be considered for the analysis.

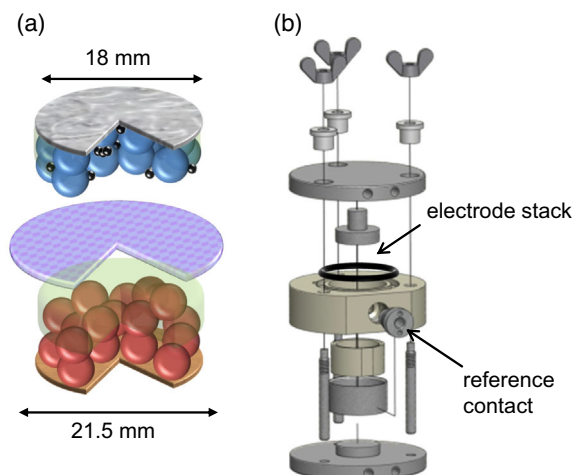


Figure 4. Three-electrode setup for EIS.^[11,12] a) Electrode configuration: counter electrode—lithium metal; working electrode—NMC cathode; reference electrode—LTO-coated aluminum mesh. b) Schematic drawing of the cell setup.

Weiss WK1 180 climate test chamber. More details on the in-house-developed three-electrode setup, EIS measurements on half-cells and full cells, and sources of error are given elsewhere.^[11,12] Time invariance, linearity, and causality of the EIS spectra were assured by Kramers–Kronig testing.^[26] Afterward, all of them were analyzed by the distribution of relaxation times (distribution of relaxation times (DRT) method). DRT relies on the fact that each impedance function that obeys the Kramers–Kronig relations can be represented as an infinite number of infinitesimal differential RC elements (resistor and capacitor in parallel).^[27] This is common in system theory and also holds true for electrochemical systems such as lithium-ion batteries. The DRT is a representation of the measured impedance $Z(\omega)$ according to its contributions occurring with different time constants.^[28,29]

3.3.1. Electronic Conductivity σ_{el}

Single-side cathode samples S1–S4 on an Al current collector were characterized in an in-house-developed four-point measurement setup.^[30] The principle of this measurement method is to induce a current at the center of a disk-shaped electrode and to measure how the potential at its surface decreases as a function of radial distances. A resistance is calculated from the measured potential and the applied probe current in dependency from the position on the probe. Assuming a known electrode geometry (thickness and radius), the electric conductivity can be extracted from resistance as a function of the radius. In the next step, the information gained from FIB/SEM tomography (τ , ϵ), conductivity measurements (σ_{el}), and EIS/DRT are applied and fitted to a two-channel TLM.

3.4. Equivalent Circuit Analysis: Transmission Line Modeling (TLM)

A two-channel TLM^[13,27] is an equivalent circuit model that describes the impedance of the porous multiphase cathodes of

this study with an electronic path (χ_{el}) along the active material and carbon black phase and an ionic path (χ_{ion}) in the liquid electrolyte in the pores. L is the thickness of the cathode, and χ_{el} and χ_{ion} are calculated as

$$\chi_{ion} [\Omega \text{ m}^{-1}] = \frac{R_{ion}}{L} = \frac{1}{\sigma_{ion}} \cdot \frac{1}{A} \cdot \frac{\tau}{\epsilon} \quad (6)$$

$$\chi_{el} [\Omega \text{ m}^{-1}] = \frac{R_{el}}{L} = \frac{1}{\sigma_{el}} \cdot \frac{1}{A} \quad (7)$$

The charge transfer reaction takes place at the interface (c) between the active material and electrolyte. Both paths χ_{el} and χ_{ion} affect the shape and polarization of the impedance spectrum and, in the case of different conductivities, cause a distributed interface reaction. In this work, the charge transfer resistance of lithium ions at the interface was modeled by an RQ element and is described by

$$\zeta [\Omega \text{ m}] = Z_{CT} \cdot L = \frac{1}{1 + j\omega R_{CT} C_{CT}} \quad (8)$$

The solid-state diffusion in the active material was not considered in this study, as it occurred at much lower frequencies ($f_{min} = 100$ mHz). Otherwise a finite space Warburg element (FSW) has to be included in ζ .

Thus, the TLM applied in this work is represented by

$$Z_{TLM} = \frac{\chi_{ion}\chi_{el}}{\chi_{ion} + \chi_{el}} \left(L + \frac{2\kappa}{\sinh(\frac{L}{\kappa})} \right) + \kappa \frac{\chi_{ion}^2 + \chi_{el}^2}{\chi_{ion} + \chi_{el}} \coth\left(\frac{L}{\kappa}\right) \quad (9)$$

$$\kappa = \sqrt{\frac{\zeta}{\chi_1 + \chi_2}} \quad (10)$$

The model applied for cathodes S1–S4, as shown in **Figure 5**, is completed by an Ohmic resistance R_0 for the Ohmic resistance in the electrolyte-filled separator and an RQ element (resistor and constant phase element in parallel) for the contact resistance R_C between the cathode and the current collector. The model parameters and the source by which they were determined are listed in **Table 2**.

The fixed model parameters are the ionic path χ_{el} and the electronic path χ_{ion} . They can be calculated with the knowledge of the microstructure parameters porosity and tortuosity obtained by

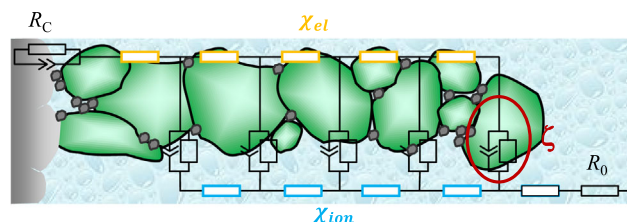


Figure 5. TLM for porous electrode structures. It considers the electronic path through the active material ($\chi_{el} = R_{el}/L$), the ionic path through the electrolyte ($\chi_{ion} = R_{ion}/L$) as in-series connected R elements, interlinked by RQ elements for the charge transfer resistance of lithium ions between the active material and electrolyte at the interface (ζ). In addition, an RQ element represents the contact resistance between the cathode and current collector and an Ohmic resistance models the loss processes in the separator.

Table 2. List of model parameters with the source by which they were determined.

Parameter	Symbol	Unit	Source
Ionic conductivity	σ_{ion}	$S\ m^{-1}$	Data sheet manufacturer
Electric conductivity	σ_{el}	$S\ m^{-1}$	Conductivity measurements
Thickness	L	M	FIB/SEM
Tortuosity	τ	–	FIB/SEM
Porosity	ϵ	%	FIB/SEM
Electrode area	A	m^2	Setup geometry
Charge transfer resistance	R_{CT}	Ω	Free fit parameter

FIB tomography, geometric parameters L and A , and electronic σ_{el} and ionic conductivity σ_{ion} , respectively (see Equation (6) and (7)), whereas χ_{ion} uses the ionic conductivity σ_{ion} value from the data sheet of the liquid electrolyte, and χ_{el} accounts for the electronic conductivity σ_{el} determined experimentally for all cathode samples.

In conclusion, the charge transfer resistance R_{CT} was obtained by a fit routine as sole free fit parameter. In **Figure 6** the impedance measurements (blue) and TLM fit results (dashed red) are shown in a Nyquist diagram exemplarily. Figure 6b shows the corresponding DRT (blue) and TLM fit results (dashed red) in a frequency plot.

The impedance spectrum of sample S3 reveals two semicircles at 1) high frequencies followed by a second one at 2) medium frequencies. At lowest frequencies 3), the capacitive contribution of the solid state diffusion in the active material started, and would continue down to the microhertz region. In this work, only the impedance contributions (1) and (2) were evaluated. The DRT indicated the existence of (up to) five characteristic time constants, which do not necessarily correspond to (up to) five “real” processes.

The impedance contributions of charge transfer and contact resistance are assigned in Figure 6 by their characteristic frequencies known from previous studies on lithium-ion electrodes published in Illig et al.^[29] and recent ones.^[31] A study with greater detail on EIS, DRT, and TLM modeling of high-energy and high-power cathodes, which were characterized at various T and SOCs, is under preparation. The contact resistance taking place at high frequencies (10^4 – 10^5 Hz) was not always as dominant as for sample S3, compared to samples S1 and S2 in Figure 9.

The charge transfer contribution was quantified after subtracting the resistance contribution of the ionic and electronic transport paths, as explained earlier. Contributions originating from electrolyte concentration gradients in the pores of the electrodes are neglected herein. The accurate fit of the measured spectrum supports the reliability of the results from microstructure analysis, as they were applied for the calculation of fixed model parameters.

4. Results and Discussion

This section presents the results of our transmission line modeling approach shown in Figure 1. First, the microstructure parameters 1) porosity ϵ , tortuosity τ , thickness L , and active surface area $a_{AM,act}$ of the cathodes obtained by FIB/SEM tomography and 2) their electronic conductivity σ_{el} are discussed and summarized in **Table 3**. Finally, 3) the charge transfer resistance R_{CT} evaluated by fitting the TLM using EIS measurements and the data given in Table 3 as well as 4) the area-specific charge transfer resistance r_{CT} of the active materials together with the resulting exchange current density j_0 and exchange coefficient k are listed and summarized in **Table 4**.

4.1. Microstructure Parameters

Figure 7 shows exemplarily three original FIB slices with an area of $\approx 38 \times 34\ \mu m^2$ and their corresponding segmented images. Herein, the white spherical areas of various sizes and inner porosities represent the active material NMC, the gray phase is the pore space, and the black phase consists of carbon black (and most probably includes the binder phase). The carbon black in S1 appears as irregular-shaped sharp agglomerates, loosely distributed in between the NMC particles. The 3D image of the reconstructed volume ($\approx 18\ 000\ \mu m^3$, with active material: green, carbon black: gray) is shown in Figure 7c and the resulting calculated microstructure parameters are given in Table 3.

Figure 7 shows the 3D reconstruction for sample S2 ($N_{0.6}M_{0.2}C_{0.2} + N_{1/3}M_{1/3}C_{1/3}$). Three original FIB slices with an area of $\approx 33 \times 26\ \mu m^2$ and their corresponding segmented image are shown in Figure 7d,e. Herein, again, the white spherical areas with uneven surface and wide agglomerate size distribution represent the active material, the gray phase is the pore space, and the black phase represents the bulky agglomerates of the carbon black. A significant part of the carbon black sticks to the surface of the NMC spheres. The 3D image of the

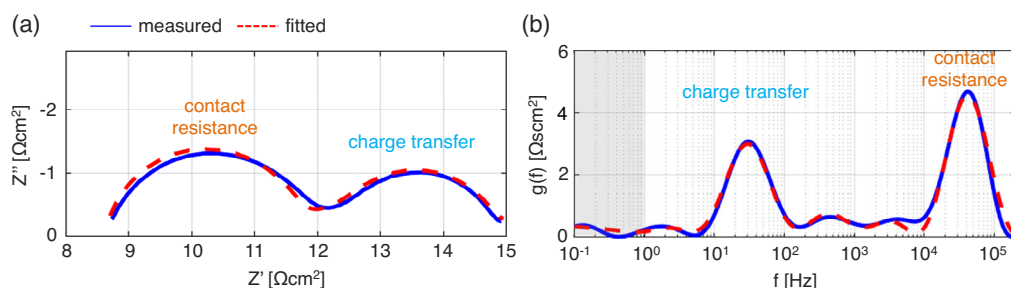


Figure 6. a) EIS measurement (SOC 100%, $T = 25\ ^\circ C$) and fit of sample S3; b) corresponding DRT and assignment of charge transfer (medium frequency range) and contact resistance (high frequency range) peaks. EIS measurements are shown by the blue lines and TLM fit by the red broken lines.

Table 3. Parameters calculated from the four cathodes.

Parameter\Sample	S1	S2	S3	S4
Layer thickness L	38 μm	47 μm	85 μm	150 μm
Porosity ϵ	43%	22%	37%	37%
Tortuosity τ	1.53	3.01	2.67	2.08
Volume-spec. active surface area $a_{\text{AM,act}}$	0.52 μm^{-1}	0.96 μm^{-1}	0.57 μm^{-1}	0.6 μm^{-1}
Total active surface area $A_{\text{AM,act}}$	50.2 cm^2	114.6 cm^2	123.1 cm^2	228.6 cm^2
Electronic conductivity σ_{el}	29.7 S m^{-1}	$1.54 \times 10^6 \text{ S m}^{-1}$	58.2 S m^{-1}	42.5 S m^{-1}

Table 4. The charge transfer resistance R_{CT} , the area specific charge transfer resistance r_{CT} , the exchange current density j_0 , and the exchange coefficient k of the investigated NMC cathodes.

Parameter	Sample			
	S1 $\text{N}_{1/3}\text{M}_{1/3}\text{C}_{1/3}$	S2 $\text{N}_{0.6}\text{M}_{0.2}\text{C}_{0.2} + \text{N}_{1/3}\text{M}_{1/3}\text{C}_{1/3}$	S3 $\text{N}_{0.6}\text{M}_{0.2}\text{C}_{0.2}$	S4 $\text{N}_{0.6}\text{M}_{0.2}\text{C}_{0.2}$
R_{CT} [Ω]	1.27	0.64	0.94	0.54
r_{CT} [$\Omega \text{ cm}^2$]	63.97	73.92	115.71	123.71
j_0 [A m^{-2}]	4.00	3.47	2.22	2.08
k [m s^{-1}]	7.38E-09	6.40E-09	4.08E-09	3.82E-09

reconstructed volume ($\approx 10\,300 \mu\text{m}^3$, with active material: green, carbon black: gray) is shown in Figure 7f and the corresponding microstructure parameters in Table 3. Sample S2, which was selected from a commercial 18 650 cell, has among all four samples the lowest porosity ($\epsilon = 22\%$) and thus the highest tortuosity ($\tau = 3.01$), as well as the highest electronic conductivity ($\sigma_{\text{el}} = 1.54 \times 10^6 \text{ S m}^{-1}$). Moreover, a mix of small-sized and large-sized partially broken NMC agglomerates cause by far the highest active surface area density ($a_{\text{AM,act}} = 0.96 \mu\text{m}^{-1}$) of all cathodes (These characteristics are advantageous, i.e., for fast charging, but of no relevance for this work).

Samples S3 (Figure 8) and S4 (Figure 8) are nominally of the same chemical composition, but of different thicknesses L . The spherical NMC agglomerates are similar in shape to S1. The 3D images display their reconstructed volumes ($\approx 41\,300$ and $18\,500 \mu\text{m}^3$). The corresponding microstructure parameters, compared to S1, are slightly lower in porosity ($\epsilon = 37\%$) and slightly higher in specific active surface area ($a_{\text{AM,act}} = 0.57$ and $0.6 \mu\text{m}^{-1}$). Understandably, the total active surface $A_{\text{AM,act}}$ differs by more than 400% among all four samples, with $A_{\text{AM,act}} = 50.2 \text{ cm}^2$ (S1) to $A_{\text{AM,act}} = 228.6 \text{ cm}^2$ (S4), due to layer thicknesses spreading from $38 \mu\text{m}$ (S1) to $150 \mu\text{m}$ (S4).

4.2. Charge Transfer Resistance R_{CT}

The acquired microstructure parameters L , ϵ , τ , as well as the electrode area A , σ_{el} , and σ_{ion} are the fixed TLM model parameters, following Equation (6) and (7). The measured half-cell impedance spectra (blue) of cathodes made from S1–S4 are displayed in a Nyquist plot in Figure 9, their corresponding DRTs

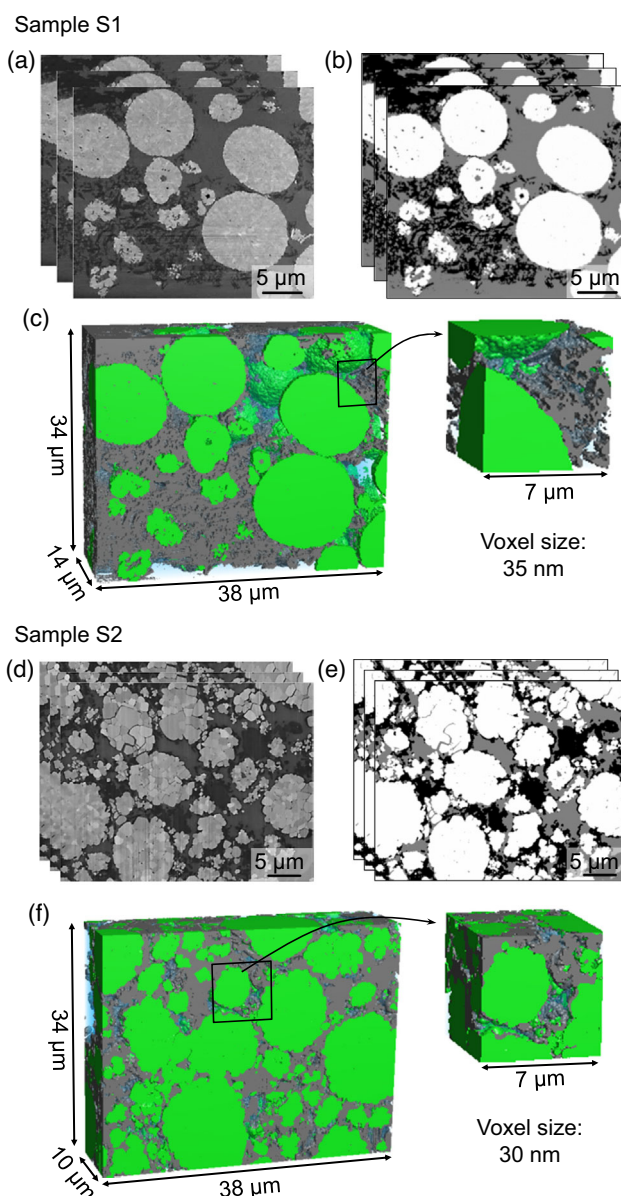


Figure 7. Samples S1 ($\text{N}_{1/3}\text{M}_{1/3}\text{C}_{1/3}$) and S2 ($\text{N}_{0.6}\text{M}_{0.2}\text{C}_{0.2} + \text{N}_{1/3}\text{M}_{1/3}\text{C}_{1/3}$). a,d) Original FIB slices, b,e) segmented images (white: active material; gray: pore; black: carbon black), and c,f) 3D representation of the reconstructed volume.

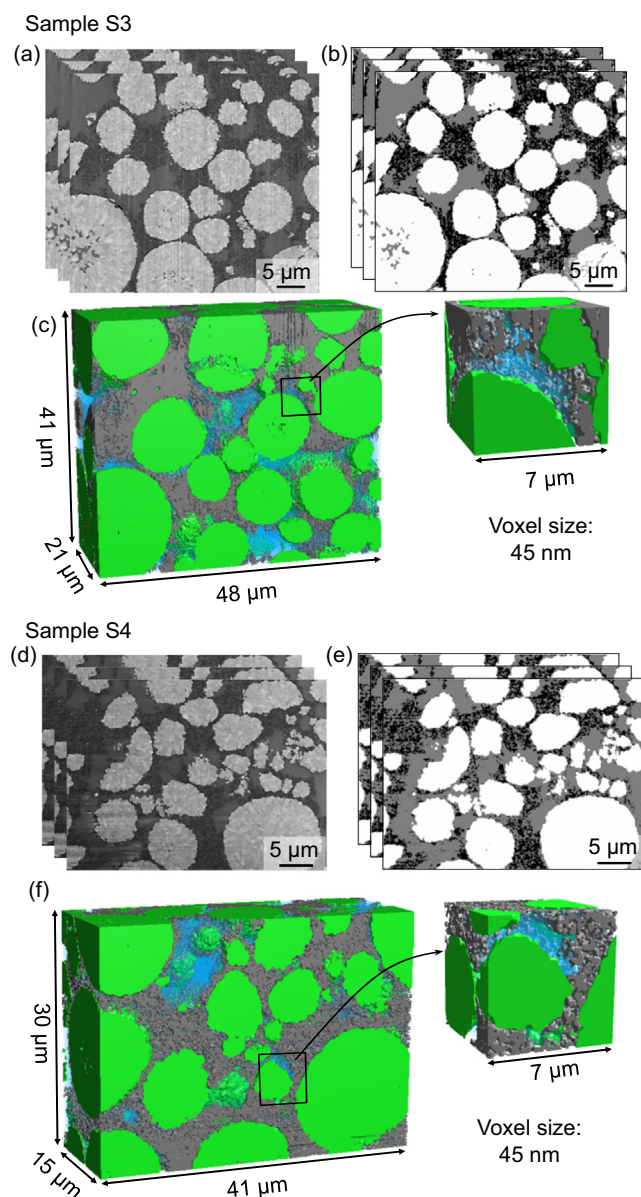


Figure 8. Samples S3 ($\text{N}_{0.6}\text{M}_{0.2}\text{C}_{0.2}$) and S4 ($\text{N}_{0.6}\text{M}_{0.2}\text{C}_{0.2}$). a,d) Original FIB slices, b,e) segmented images (white: active material; gray: pore; black: carbon black), and c,f) 3D representation of the reconstructed volume.

(blue) are shown in a frequency plot, and the individually calculated TLM fits are represented by red broken lines in both plots. It should be noted that only the frequency range relevant for charge transfer characteristics and the contact resistance are plotted, as diffusion characteristics at lower frequencies are beyond the scope of this study. The EIS plots of S1–S4 differ significantly in curve shape and size of total impedance, which is caused by a variance in cathode thickness and microstructure characteristics among the samples, whereas the DRT reveals the finer points. Herein, the impedance of samples S1 and S2 is clearly dominated by the charge transfer process, whereas in S3 and S4 the contact resistance pronouncedly contributes to the total impedance. The TLM fit always describes the course of measured

EIS data and the calculated DRT satisfactorily. As explained earlier, the parameter of interest is the free variable total charge transfer resistance R_{CT} (see Table 4). As expected, this variable spreads by a factor of 2.3 (from $R_{\text{CT}} = 0.54$ to 1.27Ω), but corresponds to the differences in thickness L and specific active surface area $a_{\text{AM,act}}$. S2 realizes $R_{\text{CT}} = 0.64 \Omega$ mainly by a high specific surface area $a_{\text{AM,act}} = 0.96 \mu\text{m}^{-1}$ and S4 (0.54Ω) by the thickest active material layer $L = 150 \mu\text{m}$.

Thus, it becomes obvious that a microstructure-independent charge transfer resistance parameter r_{CT} has to be introduced, where $r_{\text{CT}} = R_{\text{CT}} \cdot A_{\text{AM,act}}$ represents the characteristics of the active material. Finally, the remaining charge transfer parameters exchange current density j_0 and exchange coefficient k can be calculated using the parameters R_{CT} and $A_{\text{AM,act}}$ and EIS data applying Equation (4) and (5) (see Figure 9 and Table 4).

It turns out that the exchange current density j_0 ranges from 2.08 A m^{-2} (S4) $< 2.22 \text{ A m}^{-2}$ (S3) $< 3.47 \text{ A m}^{-2}$ (S2) $< 4.00 \text{ A m}^{-2}$ (S1) and the exchange coefficient k spreads from $3.85 \cdot 10^{-9} \text{ m s}^{-1}$ (S4) $< 4.08 \cdot 10^{-9} \text{ m s}^{-1}$ (S3) $< 6.40 \cdot 10^{-9} \text{ m s}^{-1}$ (S2) $< 7.38 \cdot 10^{-9} \text{ m s}^{-1}$ (S1). S3 and S4, nominally of the same chemical composition, are fairly close to each other, with a smaller deviation $\pm 7\%$ in j_0 and k . This was hoped for, as the influence of all microstructure parameters are (in the ideal case) eliminated. The single-phase active material cathodes S1, and on the other hand S3 and S4, deviate by a factor of 2. S1 owns a higher Mn and Co and a lower Ni concentration, which obviously makes the difference. S3 and S4 are nearly congruent, which is ruled by nominally the same stoichiometry. Surprisingly, even the blend cathode S2 (chemically a blend of S1 and S3 (or S1 and S4)) matches perfectly in between with its values for parameters j_0 and k , and for r_{CT} .

This work even uncovers the influence of small stoichiometry deviations within the common NMC active materials and proves the validity of a new approach for the extraction of charge transfer parameters j_0 , k , and r_{CT} . For a methodological evaluation of our new approach, a comparison with values of the exchange current density j_0 obtained from the literature was conducted. In **Figure 10**, we have assembled the NMC solid solutions (open circles) and also $\text{Ni}_{0.6}\text{Co}_{0.4}$ (diamond), LiMn_2O_4 (rectangles), and C_6 (triangles) with our own measurement results for S1–S4 (filled blue circles).

First, the variance obtained by our new approach appears small, as samples S1, S2, S3, and S4 are very close together. Nevertheless the exchange current density of $\text{Ni}_{1/3}\text{M}_{1/3}\text{C}_{1/3}$ is superior to that of $\text{N}_{0.6}\text{M}_{0.2}\text{C}_{0.2}$ and, naturally, to a blend thereof. Among the available (few) literature values for NMC solid solutions (open circles), three out of four data points are in the same dimension. The literature study^[9] of the active material $\text{Ni}_{0.4}\text{Co}_{0.6}$, evaluated in a commercial cathode by a geometrical estimation of the active surface area $A_{\text{AM,act}}$, yields similar values of $j_0 = 2.23 \text{ A m}^{-1}$ and $k = 9.53 \cdot 10^{-9} \text{ m s}^{-1}$ to the presented results for $\text{N}_{0.6}\text{M}_{0.2}\text{C}_{0.2}$.

Second, when comparing the results of this study for NMC to values of the exchange current density for $\text{LiNi}_{0.6}\text{Co}_{0.4}$ and C6 it becomes obvious that literature values of j_0 often spread over several orders of magnitude, demonstrating that the determination is very difficult and error-prone.

This work shows that a large measuring expenditure and diligent evaluation of the measurement results are necessary

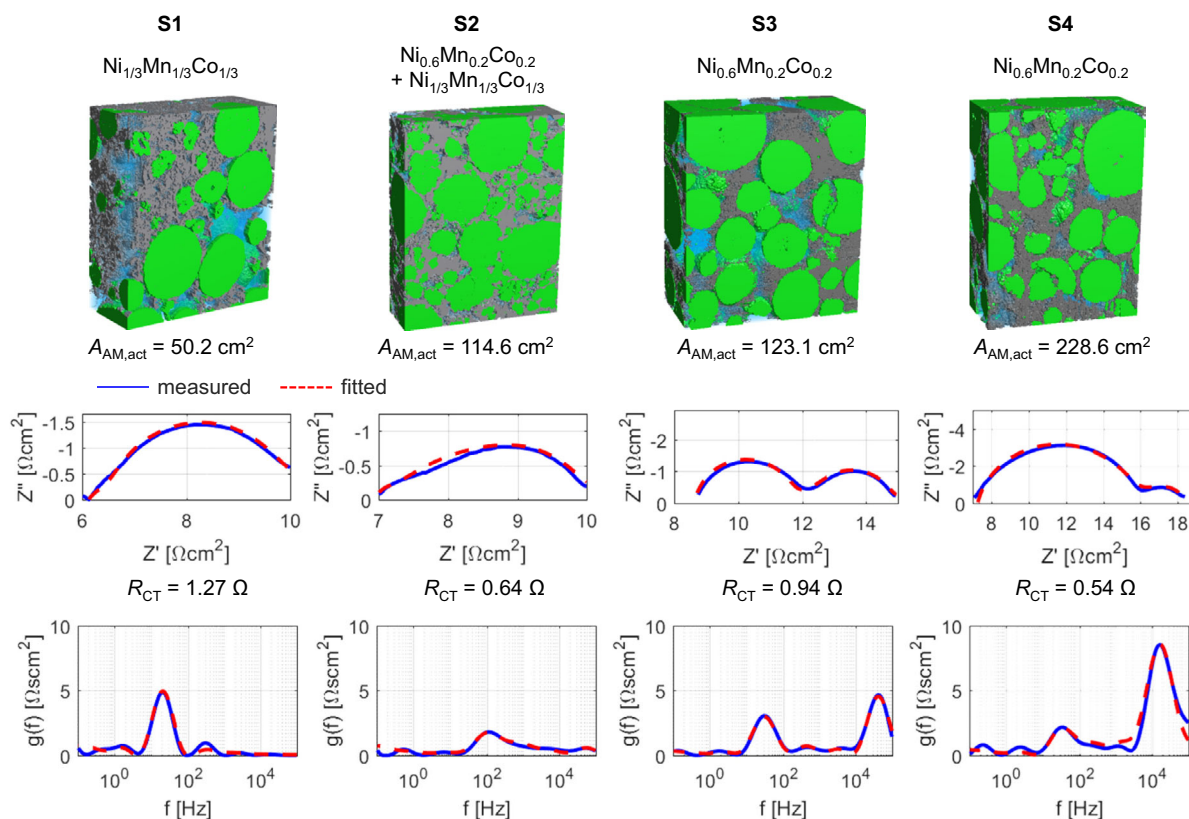


Figure 9. 3D reconstruction by FIB/SEM tomography with determined active surface area $A_{AM,act}$. Middle and bottom: EIS impedance displayed in Nyquist diagrams and the corresponding calculated DRT (blue lines). The resulting TLM fits using the relevant parameters are in very good agreement (red lines) and the determined charge transfer resistances R_{CT} for samples S1–S4 are given below the impedances.

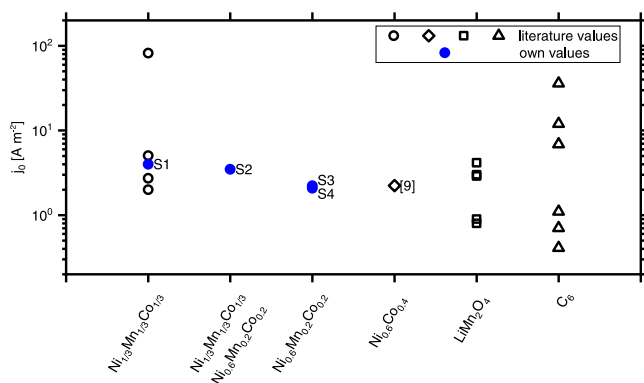


Figure 10. Comparison of the results of this study for the exchange current density (blue) and values from the literature (black) for $Ni_{1/3}Mn_{1/3}Co_{1/3}$,^[3,15,33,34] $Ni_{0.6}Mn_{0.2}Co_{0.2}$,^[9,35] $Ni_{0.4}Co_{0.6}$,^[9,35] $LiMn_2O_4$,^[10,36–39] and C_6 (graphite).^[3,37–40]

for obtaining these parameters. The reliability of the results is shown by the low deviation of all four cathodes with quite different microstructure features. The accuracy of the presented set of microstructure parameters could be further improved by examining an even larger volume for the microstructure reconstruction.^[8,22] A promising approach therefore could be the combination of X-ray and FIB, which was suggested by

Zielke et al.^[32] In this way, the microstructure could be investigated on multiple length scales with different resolutions. We are preparing a paper pursuing this approach for NMC cathodes examined by FIB/SEM and μ CT analysis.

5. Conclusion

A new approach has been demonstrated for obtaining the following parameters of lithium-ion battery cathodes: exchange current density j_0 , exchange coefficient k , and area-specific charge transfer resistance r_{CT} . In this study, either electrode sheets composed of a single-phase material ($Ni_{1/3}Mn_{1/3}Co_{1/3}$ and $Ni_{0.6}Mn_{0.2}Co_{0.2}$) are examined or one blend thereof ($Ni_{0.6}Mn_{0.2}Co_{0.2} + Ni_{1/3}Mn_{1/3}Co_{1/3}$).

Our approach relies on the following three experimental methods combined with a TLM for porous electrodes. 1) The microstructural parameters tortuosity τ , porosity ϵ , and active surface area $A_{AM,act}$ of the NMC particles in the NMC sheets are obtained by FIB/SEM tomography data analysis. Because state-of-the-art cathodes consist of large micrometer-sized active material particles mixed with significantly smaller nanometer-sized carbon black particles (and agglomerates thereof), pixel sizes between 30 and 45 nm were used to make the carbon black phase visible. Indeed, representative volumes between 10 071 and 41 328 μm^3 were reconstructed (among the largest reconstructions via FIB/SEM tomography reported in the literature).

2) The effective electronic conductivity σ_{el} of the NMC sheets was measured by a four-point measurement setup. 3) The complex impedance of all NMC sheets was measured in a three-electrode setup by EIS.

Afterward, the absolute charge transfer resistances R_{CT} of the different NMC cathodes were quantitatively determined using the DRT in combination with a TLM for porous electrode structures. For reliability, it is essential to apply the results of FIB tomography and conductivity measurements (τ , ϵ , σ_{el}) in this complex impedance model.

Finally, the area-specific charge transfer resistance r_{CT} is gained for all NMC stoichiometries by correlating the respective values of the active surface area $A_{AM,act}$ (FIB/SEM tomography) and the total charge transfer resistance R_{CT} (EIS measurements). This is a precondition for calculating the exchange current density j_0 and the exchange coefficient k using the equations given in the text. The parameter k is independent of the microstructure and SOC, and is of great importance for homogenized porous electrode models, i.e., the Newman model.

Considering the potential error sources of the experimental methods used, the presented new approach is validated because it yields consistent results among the investigated NMC stoichiometries and negligible deviations for nominally equal stoichiometries. Furthermore, four representative parameter sets of r_{CT} , j_0 , and k are delivered for the performance modeling of NMC cathodes. Naturally, this new approach is transferable to a series of relevant electrode active materials.

Acknowledgements

J.C., J.J., and A.S. contributed equally to this work. The authors would like to thank Kazuya Takeuchi (Toyota Motors Corporation, currently a guest researcher at KIT) for his invaluable support and Jake Packham for proof-reading. This work was funded by the Deutsche Forschungsgemeinschaft (DFG) in the framework of the research training group SIMET (281041241/GRK2218) and by the Friedrich-und-Elisabeth-Boysen-Stiftung (BOY-121). Open access funding enabled and organized by Projekt DEAL.

Conflict of Interest

The authors declare no conflict of interest.

Keywords

charge transfer kinetics, electrochemical modeling, exchange current density, focused ion beam tomography, lithium-ion cathodes, transmission line models

Received: October 2, 2020

Revised: December 9, 2020

Published online:

[1] J. Newman, W. Tiedemann, *AIChE J.* **1975**, *21*, 25.

[2] A. Schmidt, E. Ramani, T. Carraro, J. Joos, A. Weber, M. Kamlah, E. Ivers-Tiffée, *Energy Technol.* **2020**, <https://doi.org/10.1002/ente.202000881>.

- [3] Y. Ji, Y. Zhang, C.-Y. Wang, *J. Electrochem. Soc.* **2013**, *160*, A636.
 [4] J. Lück, A. Latz, *Phys. Chem. Chem. Phys.* **2019**, *21*, 14753.
 [5] N. Lin, F. Röder, U. Krewer, *Energies* **2018**, *11*, 2998.
 [6] S. Cernak, F. Gerbig, M. Kespe, H. Nirschl, *Energy Storage* **2020**, *2*, e156.
 [7] M. Ender, J. Joos, T. Carraro, E. Ivers-Tiffée, *J. Electrochem. Soc.* **2012**, *159*, A972.
 [8] L. Almar, J. Joos, A. Weber, E. Ivers-Tiffée, *J. Power Sources* **2019**, *427*, 1.
 [9] M. Ecker, T. K. D. Tran, P. Dechent, S. Käbitz, A. Warnecke, D. U. Sauer, *J. Electrochem. Soc.* **2015**, *162*, A1836.
 [10] A. K. Hjelm, G. Lindbergh, *Electrochim. Acta* **2002**, *47*, 1747.
 [11] M. Ender, J. Illig, E. Ivers-Tiffée, *J. Electrochem. Soc.* **2017**, *164*, A71.
 [12] J. Costard, M. Ender, M. Weiss, E. Ivers-Tiffée, *J. Electrochem. Soc.* **2017**, *164*, A80.
 [13] J. Euler, W. Nonnenmacher, *Electrochim. Acta* **1960**, *2*, 268.
 [14] J. S. Newman, K. E. Thomas-Alyea, *Electrochemical Systems*, Wiley, Hoboken, NJ **2004**.
 [15] J. Schmalstieg, C. Rahe, M. Ecker, D. U. Sauer, *J. Electrochem. Soc.* **2018**, *165*, A3799.
 [16] T. R. Ijsselstein, Diploma Thesis, KIT **2015**.
 [17] D. Andre, S.-J. Kim, P. Lamp, S. F. Lux, F. Maglia, O. Paschos, B. Stiaszny, *J. Mater. Chem. A* **2015**, *3*, 6709.
 [18] J. R. Wilson, J. S. Cronin, S. A. Barnett, S. J. Harris, *J. Power Sources* **2011**, *196*, 3443.
 [19] M. Ender, J. Joos, T. Carraro, E. Ivers-Tiffée, *Electrochem. Commun.* **2011**, *13*, 166.
 [20] J. Joos, T. Carraro, A. Weber, E. Ivers-Tiffée, *J. Power Sources* **2011**, *196*, 7302.
 [21] P. R. Shearing, J. Golbert, R. J. Chater, N. P. Brandon, *Chem. Eng. Sci.* **2009**, *64*, 3928.
 [22] J. Joos, M. Ender, T. Carraro, A. Weber, E. Ivers-Tiffée, *Electrochim. Acta* **2012**, *82*, 268.
 [23] M. Ender, J. Joos, A. Weber, E. Ivers-Tiffée, *J. Power Sources* **2014**, *269*, 912.
 [24] T. Hutzenlaub, S. Thiele, R. Zengerle, C. Ziegler, *Electrochem. Solid-State Lett.* **2012**, *15*, 2.
 [25] Z. Liu, J. Scott Cronin, Y. C. K. Chen-Wiegart, J. R. Wilson, K. J. Yakal-Kremiski, J. Wang, K. T. Faber, S. A. Barnett, *J. Power Sources* **2013**, *227*, 267.
 [26] M. Schönleber, D. Klotz, E. Ivers-Tiffée, *Electrochim. Acta* **2014**, *131*, 20.
 [27] R. de Levie, *Electrochim. Acta* **1964**, *9*, 1231.
 [28] H. Schichlein, A. C. Muller, M. Voigts, A. Krugel, E. Ivers-Tiffée, *J. Appl. Electrochem.* **2002**, *32*, 875.
 [29] J. Illig, M. Ender, A. Weber, E. Ivers-Tiffée, *J. Power Sources* **2015**, *282*, 335.
 [30] M. Ender, A. Weber, E. Ivers-Tiffée, *Electrochem. Commun.* **2013**, *34*, 130.
 [31] M. Weiss, Ph.D. Thesis, KIT **2020**.
 [32] L. Zielke, T. Hutzenlaub, D. R. Wheeler, C. W. Chao, I. Manke, A. Hilger, N. Paust, R. Zengerle, S. Thiele, *Adv. Energy Mater.* **2015**, *5*, 1401612.
 [33] L. Wang, J. Zhao, X. He, J. Gao, J. Li, C. Wan, C. Jiang, *Int. J. Electrochem. Sci.* **2012**, *7*, 345.
 [34] S. Tippmann, Ph.D. thesis, Universität Stuttgart **2016**.
 [35] M. Ecker, S. Käbitz, I. Laresgoiti, D. U. Sauer, *J. Electrochem. Soc.* **2015**, *162*, A1849.
 [36] M. Mohamedi, D. Takahashi, T. Uchiyama, T. Itoh, M. Nishizawa, I. Uchida, *J. Power Sources* **2001**, *93*, 93.
 [37] T. F. Fuller, *J. Electrochem. Soc.* **1994**, *141*, L21.
 [38] P. Arora, M. Doyle, A. S. Gozdz, R. E. White, J. Newman, *J. Power Sources* **2000**, *88*, 219.
 [39] M. Doyle, Y. Fuentes, *J. Electrochem. Soc.* **2003**, *150*, A706.
 [40] M. Doyle, *J. Electrochem. Soc.* **1996**, *143*, 1890.